Research paper

Wave energy assessment based on reanalysis data calibrated by buoy observations in the southern South China Sea

Bo Li [a,b,c], Wuyang Chen [a,d], Junmin Li [a,b,c,*], Junliang Liu [a], Ping Shi [a,c], Huanlin Xing [a]

[a] *State Key Laboratory of Tropical Oceanography, Key Laboratory of Science and Technology on Operational Oceanography, Guangdong Key Laboratory of Ocean Remote Sensing, Guangdong Provincial Observation and Research Station for Coastal Upwelling Ecosystem, South China Sea Institute of Oceanology, Chinese Academy of Sciences, Guangzhou 511458, China*
[b] *Sanya Institute of Oceanology, South China Sea Institute of Oceanology, Chinese Academy of Sciences, Sanya 572025, China*
[c] *Southern Marine Science and Engineering Guangdong Laboratory (Guangzhou), Guangzhou 511458, China*
[d] *School of Electronics and Information Engineering, Guangdong Ocean University, Zhanjiang 524025, China*

ARTICLE INFO

ABSTRACT

This study assesses wave energy by combining long-term model reanalysis data with in situ observations in a multi-island region. A buoy was deployed in the center area of the southern South China Sea (SCS) for 16 consecutive months. Neural network models are introduced to calibrate the significant wave height and the mean wave period of the European Center for Medium-Range Weather Forecasts (ECMWF) ERA5 reanalysis data. Based on the calibrated reanalysis data, wave energy potential in the region is assessed. The results show relatively available wave resources from October to February in climatology, with an average energy density higher than 5 kW m^{-1} and an available level frequency higher than 50%. Wave energy potential is relatively poor in other months. In the last 40 years, the wave energy density, available level frequency, and rich level frequency have shown significant increasing trends, consistent with the wind enhancement in the northeast SCS. It is suggested that the growth trend of waves in the northeast SCS may spread to the south region as swell propagation. The analysis emphasizes that there can be significant differences in the results of wave energy assessments, whether the data are calibrated or not. Therefore, the data accuracy needs to be fully evaluated when adopting model results for the planning and utilization of wave energy in such region.

1. Introduction

In recent years, the development and utilization of clean, pollution-free, and renewable energy have attracted much attention. Wave energy has certain distinct advantages because it has a high and concentrated flux density (Pérez-Collazo et al., 2015). The global potential reserve of wave energy has been estimated at approximately 2 TW (Gunn and Stockwilliams, 2012), which can strongly meet the demand for the development and utilization of sea resources far from the mainland. For example, wave energy is expected to support the development of remote islands and reefs in the South China Sea (SCS) (Zheng and Li, 2015) in multiple fields, such as marine ranches, drilling platforms, and scientific equipment.

It is important to evaluate the wave power potential and its variabilities before planning energy utilization programs. Adequate wave energy assessments have been performed in the SCS,

depending on the significant wave height (*Hs*), etc. provided by numerical models (Zheng et al., 2012, 2013; Ali et al., 2015; Lin et al., 2019; Sun et al., 2020) and/or the corresponding reanalysis product (Wan et al., 2015, 2018; Wang et al., 2018). However, in the southern SCS (SSCS) (Fig. 1), a large number of islands and reefs would significantly influence the wave dynamics by the shading effect (Andréfouët et al., 2012; Fett and Kevin, 1976; Li et al., 2022b; Ponce de León and Soares, 2005). The distribution and variation of the wave energy would be blocked by the island groups (Ali et al., 2015; Sun et al., 2020). As a result, common wave models might not be complicated enough to characterize the coexistence of swells from the open sea and local waves affected by complex bathymetry in multi-island regions (Sun et al., 2021), probably due to the limitation of spatial resolution (Tolman, 2003; Mao et al., 2014). Moreover, most satellite products are unable to provide wave period data, which is indispensable in wave energy calculation. Although in situ observations have been used to calculate wave power directly (Chen et al., 2017) or to verify the modeling data for further energy assessment (Zheng et al., 2013; Wan et al., 2015, 2018; Lin et al., 2019), most of them are confined to the northern China seas with relatively short measuring periods. Studies combining in situ observations with

* Corresponding author at: State Key Laboratory of Tropical Oceanography, South China Sea Institute of Oceanology, Chinese Academy of Sciences, Guangzhou 511458, China.
E-mail address: jli@scsio.ac.cn (J. Li).
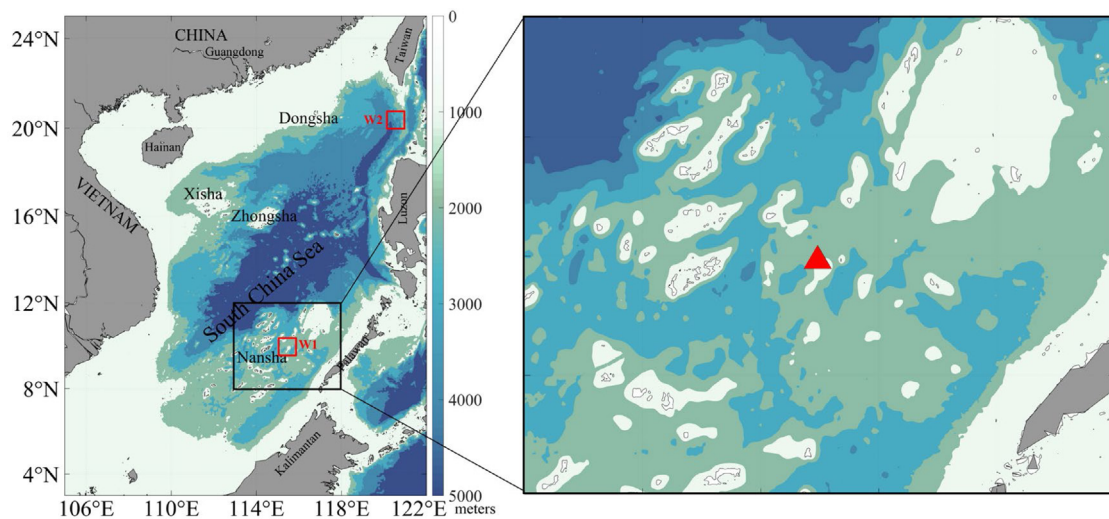
Fig. 1. Geography and bathymetry of the South China Sea and the study site (red triangle) for the wave energy assessment. The two red boxes (W1 and W2) in the left panel correspond to the calculation region for the annual variations of wind speed in Fig. 11. (For interpretation of the references to color in this figure legend, the reader is referred to the web version of this article.)

long-series model data to assess the wave energy in multi-island regions in the SSCS are a desideration task at present.

The long-term variation of wave energy and its dynamic mechanism have been emphasized by scientists. Increasing studies have been carried out on the long-term trend of wave energy in the Northwestern Pacific (Bromirski et al., 2013; Zheng and Li, 2015), North Atlantic (Reeve et al., 2011), the Persian Gulf (Kamranzad et al., 2013), Europe (Iglesias et al., 2009; Emmanouil et al., 2016), and even the global oceans (Young et al., 2011; Zheng, 2021). Most of them pointed out that the increase in the frequency of gale events is the main reason for the rise of global wave height and wave energy resources (Reeve et al., 2011; Young et al., 2011; Zheng, 2021). However, in some unique areas such as the SSCS, the long-term trend of wave energy and its relation with the variation of wind field still need to be clarified based on more accurate data.

Notably, artificial neural networks (ANNs) have been widely used to develop wave forecasting models or to improve wave parameter hindcasts for decades (Deo and Naidu, 1998; Guenaydin, 2008; Li et al., 2020). Recently, several wave energy assessments have been implemented making use of the ANN method in different regions, such as the Canary Islands in the North Atlantic (Avila et al., 2020), Brazil's coast of the Atlantic (Sánchez et al., 2018), the Caspian Sea (Hadadpour et al., 2014), the Pacific and Atlantic coasts, and the Gulf of Mexico (Reikard et al., 2011; Bento et al., 2021). These studies showed that the developed models based on ANNs constitute an efficient tool to simulate wave power quickly and accurately near coastal oceanic waters (Avila et al., 2020), making optimal use of in situ measurements to characterize the wave energy resources of coastal sites (Sánchez et al., 2018), especially in the short-term assessment of wave resources (Reikard et al., 2011; Bento et al., 2021). In particular, the combination of the physics-based model and ANN yields more accurate wave energy simulations than either model alone (Reikard et al., 2011). Moreover, wave energy fluxes calculated with ANN-calibrated wave parameters are more accurate than the direct forecast of the energy flux (Hadadpour et al., 2014). Therefore, ANNs can provide a promising tool for calibrating model data to accurately assess wave energy resources in multi-island regions. Compared with the traditional quantile mapping method (Wood et al., 2002; Thrasher et al., 2012) which corrects the modeling results by establishing a transfer function assuming that the observed and simulated values are subject to specific

probability distributions, the advantage of the proposed method in this study is that more factors related to the target variable can be considered. Through machine learning, our method can establish an optimum relationship between multiple input factors and the target variable without relying on given formulas.

This study provides an example of wave energy assessment in a multi-island region of the SSCS based on a combination of long-term model data and field observations by the ANN method. A typical study site (10.0°N, 115.5°E) with 1200 m depth was set up in the central area of the Nansha Islands region (Fig. 1). A buoy was deployed at the site for 16 consecutive months. The ERA5 model data of 1979–2020 were calibrated by the buoy data and then used to calculate wave energy parameters. The importance of calibrated data for the assessment was further verified by comparing the results of calibrated data with those of original model data.

2. Data and methods

2.1. Reanalysis data and buoy observations

The ECMWF ERA5 reanalysis data, including significant wave height (Hs), mean wave period (Tm), mean wave direction ($Mdir$), wind velocity ($Wvel$), and wind direction ($Wdir$) at the study site (Fig. 1) were obtained for further analysis. There are a total of 363 048 groups of data (Hs, Tm, $Mdir$, $Wvel$, and $Wdir$) at one-hour intervals, starting from January 1979 to May 2020. ERA5 is the fifth generation ECMWF reanalysis of the global climate and weather (Hersbach et al., 2018), providing hourly estimates on single levels for a large number of atmospheric, ocean-wave, and land-surface quantities. It can be downloaded from the website http://climate.copernicus.eu/climate-reanalysis.

Regarding the document of ECMWF ocean wave model output parameters (ECMWF, 2021), the Hs is defined as $Hs \equiv 4\sqrt{m_0}$, in which m_n is the nth moment of spectral density. The Tm is defined as $Tm \equiv Tm_{-10} = m_{-1}/m_0$ which is also commonly known as the energy mean wave period (Te, ERA5 Tm is collectively referred to as Te hereinafter). Together with Hs, it can be used to determine the wave power. Although the data combine a vast number of historical observations into global estimates using advanced modeling and data assimilation systems, few wave observations in the SCS are available for the assimilation of the model. There
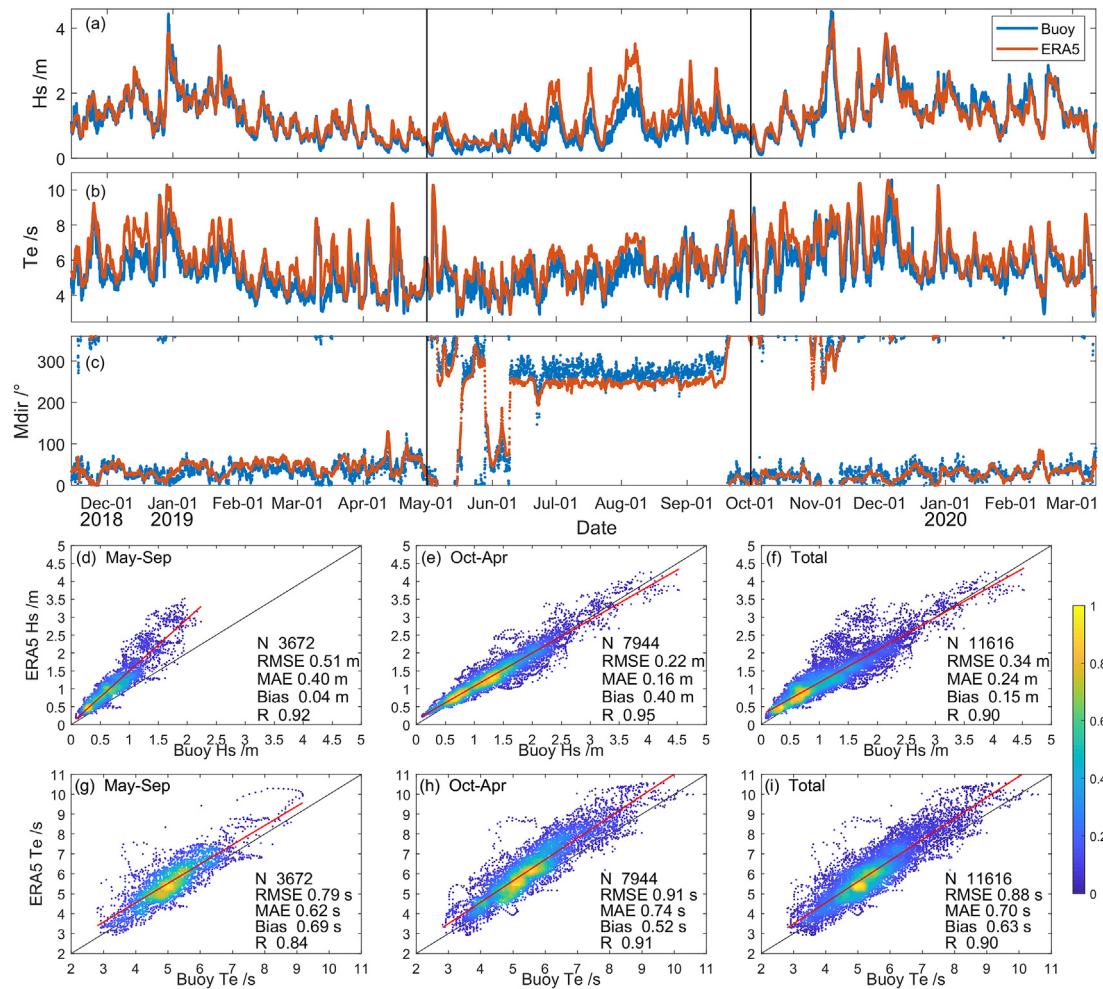
Fig. 2. Comparisons of wave parameters from the buoy and ERA5. Upper panels are the time series of (a) *Hs*, (b) *Te*, and (c) *Mdir*. Lower panels are scattered plots of (d–f) *Hs* and (g–i) *Te* during (d, g) the summer monsoon period, (e, h) the rest period, and (f, i) the whole observation period. In the upper panels (a–c), the vertical lines separate the summer monsoon season and the rest season. In lower panels (d–f), the color indicates the percentage density of the scattered plots, and the red line is a linear fitting curve of the scattered plots. (For interpretation of the references to color in this figure legend, the reader is referred to the web version of this article.)

is not even a long-term buoy in the whole SCS deployed by the NOAA National Data Buoy Center.

A wave buoy was deployed at the study site (Fig. 1) on November 14, 2018, and 16 months of data were measured as of March 12, 2020. A Triaxys wave sensor manufactured by AXYS Technologies Inc., Canada, was equipped in the buoy to measure wave parameters, i.e., *Hs*, *Tm*, and *Mdir*, every hour by the gravitational acceleration method (Macisaac and Naeth, 2014).

In general, the buoy-observed wave period is not specified in terms of the energy period *Te*. *Te* can be estimated by the formula $Te = \alpha Tp$, where *Tp* is the peak period, and α depends on the shape of the wave spectrum defining the sea state (Cornett, 2008). However, the *Tp* of the wave spectrum obtained through discrete frequency has a runout, that is, unstable. Instead, the buoy calculated the mean wave period *Tm* based on the second moment of the spectrum Tm_{02}, which is also known as the zero-crossing period (*Tz*) as it corresponds to the mean period that is determined from observations of the sea surface elevation using the zero-crossing method. The relationship between *Tm* and *Tp* is approximately given as $Tp = 1.2Tm$ (Bedard, 2009; Zheng et al., 2012; Wu et al., 2015; Chen et al., 2017). In this study, we adopt a conservative approximation that $\alpha = 0.9$, assuming that the sea state in the SSCS is subjected to a standard JONSWAP

spectrum. This assumption was used in wave power assessment in the global ocean (Cornett, 2008), as well as in the offshore waters of the China seas (Wu et al., 2015; Chen et al., 2017). Consequently, *Te* from the real sea state is estimated by the buoy observation as:

$$Te = 0.9 \times 1.2Tm = 1.08Tm \qquad (1)$$

The accuracy of the ERA5 wave parameters is evaluated compared with buoy observations in Fig. 2. As illustrated in Fig. 2a–c, *Hs*, *Te*, and *Mdir* of ERA5 generally agree with the buoy observations in the variation trends. However, during the summer monsoon season from May to September 2019, the ERA5 *Hs* is larger than the observations, representing a root-mean-square error (RMSE) of 0.51 m (Fig. 2d), twice the error for the rest season from November 2018 to April 2019 and October 2019 to March 2020 (Fig. 2e). The ERA5 *Te* is relatively larger than the buoy observations throughout the whole period (Fig. 2b). There is no essential difference in the accuracy of the ERA5 *Te* during the summer monsoon and the rest time (Fig. 2g–i). Considering that both *Hs* and *Te* are essential for calculating wave energy density, they need further calibration to ensure the accuracy of wave energy assessment.
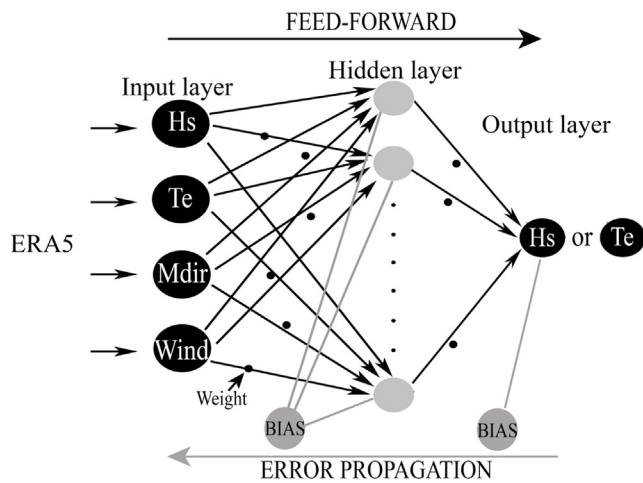
Fig. 3. The conception of the feed-forward neural network (NN).

2.2. Artificial neural network for data calibration

A multilayer feed-forward ANN is established to calibrate the ERA5 *Hs* and *Te*, combined with buoy data. As shown in Fig. 3, the network is composed of an input layer, a hidden layer, and an output layer. The information of the training samples from the input layer gradually propagates forward through the transfer function. If the output result cannot reach the expected output, the observation data and the bias between the output signal and the expected value will be returned to the input layer. Furthermore, the weight and threshold will be adjusted according to the training error so that the output will constantly approach the expected value. Finally, the weight coefficient matrix and the threshold matrix will be determined by massive repeated training. The ANN adopted the Levenberg–Marquardt backpropagation algorithm (Beale et al., 2010) for sample training by using the MATLAB neural network toolbox. After tentative computation, the number of nodes in the hidden layer was set as 8, and the training times were 3000. The hidden layer used a hyperbolic tangent sigmoid transfer function, while the output layer used a linear transfer function. Such an ANN is an efficient and mature algorithm that is widely used in the calibration, modeling, and prediction of ocean hydrological parameters (e.g., Deo and Naidu, 1998; Londhe et al., 2016; Lu et al., 2019; Li et al., 2020).

In this study, the ANN structure was optimized by fully considering possible input variables. Five ANN models were established to calibrate the ERA5 *Hs* and *Te* (Table 1). Among them, wave parameters (*Hs*, *Te*, and *Mdir*), as well as wind velocities (*Wvel*), were gradually brought into the input level. The mean wave direction and the wind vectors are decomposed into meridional components (*MdirX*, *WindX*) and latitudinal components (*MdirY*, *WindY*), respectively. Moreover, this study divided the data samples into two datasets for calibrating *Hs* since the data accuracy varies for different seasons (Fig. 2). One is May–September 2019, and the other is November 2018–April 2019 and October 2019–March 2020 (Datasets 1 and 2, Table 2). The two databases were independently selected to establish the ANN model for *Hs* during the summer monsoon and the rest periods. For *Te*, samples ranging from November 2018 to March 2020 were taken into ANN calibration (Dataset 3, Table 2). In each database, the earlier 80% of the total data is used for network training. The remaining 20% is involved in the verification of the training results. Then, the ANN models with the best calibration effect on *Hs* and *Te* can be determined.

Table 1
Variable settings of the ANN models.

Model	Input	Output
NN H1	*Hs*	*Hs*
NN H2	*Hs, Te*	*Hs*
NN H3	*Hs, Te, MdirX, MdirY*	*Hs*
NN H4	*Hs, WindX, WindY*	*Hs*
NN H5	*Hs, Te, MdirX, MdirY, WindX, WindY*	*Hs*
NN T1	*Te*	*Te*
NN T2	*Te, Hs*	*Te*
NN T3	*Te, Hs, MdirX, MdirY*	*Te*
NN T4	*Te, Hs, WindX, WindY*	*Te*
NN T5	*Te, Hs, MdirX, MdirY, WindX, WindY*	*Te*

2.3. Assessment of wave energy resource

According to the wave energy resource assessment algorithms by Cornett (2008), the wave energy density is calculated by:

$$Pw = \frac{\rho_w g^2}{64\pi} Hs^2 Te \tag{2}$$

where P_w is the wave energy density flux per unit of wave-crest length (kW m^{-1}), *Hs* is in m, and *Te* is in s. Furthermore, ρ_w is the density of seawater as 1025 kg m^{-3}, and *g* is the gravitational acceleration as 9.8 m s^{-2}.

It is important to evaluate the stability of P_w for the development and utilization of wave energy converters (WECs) because stable wave energy is advantageous to the acquisition and conversion of energy (Cornett, 2008). The wave energy stability is quantified by the coefficient of variation (*Cv*) by the formula:

$$Cv = \left[\sum_{i=1}^{N} \left(P_{wi} - \overline{P_w} \right)^2 / N \right]^{1/2} / \overline{P_w} \tag{3}$$

where $\overline{P_w}$ is the mean of P_w and *N* is the sample size of P_w.

The available level frequency (ALF) and the rich level frequency (RLF) are important criteria to measure the rich degree of wave energy resources. Zheng et al. (2013) stated that wave energy is available when the density is greater than 2 kW m^{-1}, while the region where density is greater than 20 kW m^{-1} is considered a rich area. This criterion was followed by Wan et al. (2015). In addition, they proposed that wave energy with a *Hs* being not less than 1 m or not greater than 4 m is exploitable. As some excellent wave power devices can well absorb the wave energy when the wave is higher than 0.5 m (Zheng et al., 2013), in this study, we yield to relatively moderate criteria, and ALF and RLF are defined as follows:

$$\begin{cases} \text{ALF} = \dfrac{n \left(P_w \geq 2 \text{ kW m}^{-1}, 0.5 \text{ m} \leq Hs \leq 4 \text{ m} \right)}{N} \times 100\% \\ \text{RLF} = \dfrac{n \left(P_w \geq 20 \text{ kW m}^{-1}, 0.5 \text{ m} \leq Hs \leq 4 \text{ m} \right)}{N} \times 100\% \end{cases} \tag{4}$$

where *n* is the size of samples in which *Pw* and *Hs* satisfy the corresponding criteria, and *N* is the total sample size. As the technical progress and the varying of the geographic condition, the standard indicating the abundant level of the wave energy may differ. For example, Stopa et al. (2013) expected that WECs will require 5 kW m^{-1} of *Pw* to be operational and an annual median of 12 kW m^{-1} for economic viability in Hawaii. Therefore, this criterion is also concerned in the present study.

3. Results and discussion

3.1. Calibrated result of the ERA5 data

The ANN models listed in Table 1 were performed to calibrate the *Hs* and *Te* of ERA5 data. Based on Dataset 1, calibration

Table 2
Data periods for ANN training and verification.

|	Data period	Calibrated parameter	Training period ∼80%	Verification period ∼20%
Dataset 1	May–Sep. 2019	Hs	May–Aug. 2019	Sep. 2019
Dataset 2	Nov. 2018–Apr. 2019 Oct. 2019–Mar. 2020	Hs	Nov. 2018–Apr. 2019 Oct.–Dec. 2019	Jan.–Mar. 2020
Dataset 3	Nov. 2018–Mar. 2020	Te	Nov. 2018–Dec. 2019	Jan.–Mar. 2020
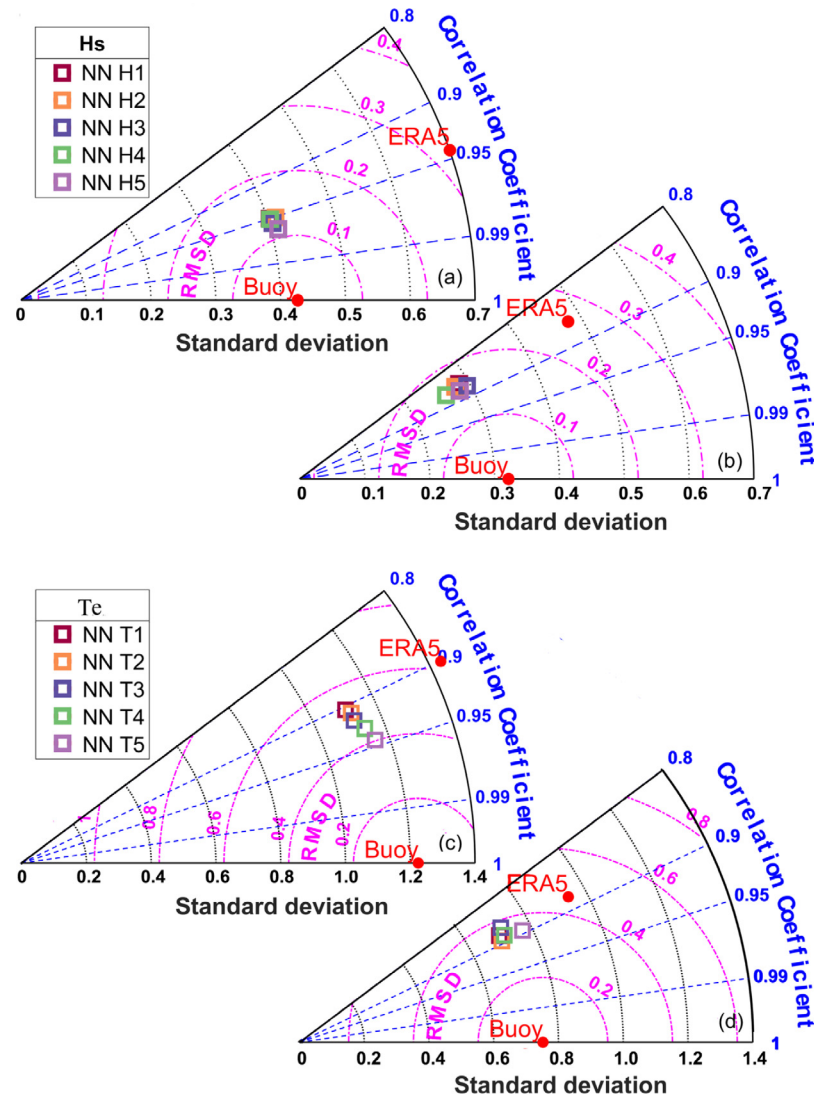
Fig. 4. Taylor diagrams of ANN models in the training stage (a, c) and the verification stage (b, d) in the calibration of *Hs* (upper panels) and *Te* (lower panels). In the figures, ERA5 indicates the results of uncalibrated model data, and buoy indicates the reference values observed by the buoy. Note that the RMSD in Taylor diagram is the centered pattern root-mean-square difference (Taylor, 2001), which is different from the root-mean-square deviation.

models for *Hs* of the summer monsoon period were trained and verified. The synchronous hourly data from ERA5 and buoy during May–August 2019 were used for training to establish models NN H1–H5. Then, the independent data of September 2019 were used to verify the models. Similarly, calibration models for *Te* during the whole observation period were established based on Dataset 3. The data during November 2018–December 2019 were used for training to establish models NN T1–T5, and the data from January–March 2020 were used to verify the models. The overall calibration performance of the ANN models in the training and verification stages is illustrated in Taylor diagrams (Fig. 4). The diagrams show that compared with the original *Hs* and *Te* of ERA5, all of the calibrated results using different ANN models

are closer to the observation values, making the centered pattern root-mean-square difference, the standard deviation, and the correlation coefficient improve significantly.

The time series with a scatter diagram of *Hs* and *Te* during the verification stage are illustrated in Figs. 5 and 6, respectively. After calibration, the RMSE of *Hs* in September 2019 decreased from 0.41 m to 0.19–0.23 m (Fig. 5). The mean absolute error and bias also decrease. In general, the NN H5 shows the best improvement. As shown in Fig. 6, *Te* calibrated by models NN T1–T5 agrees well with the field observation data in the verifying stage, with the RMSE reduced from 0.64 s to 0.39–0.48 s.

The more relevant environmental factors are considered, the more information can be brought to the neural network, which can improve the accuracy of the neural network model
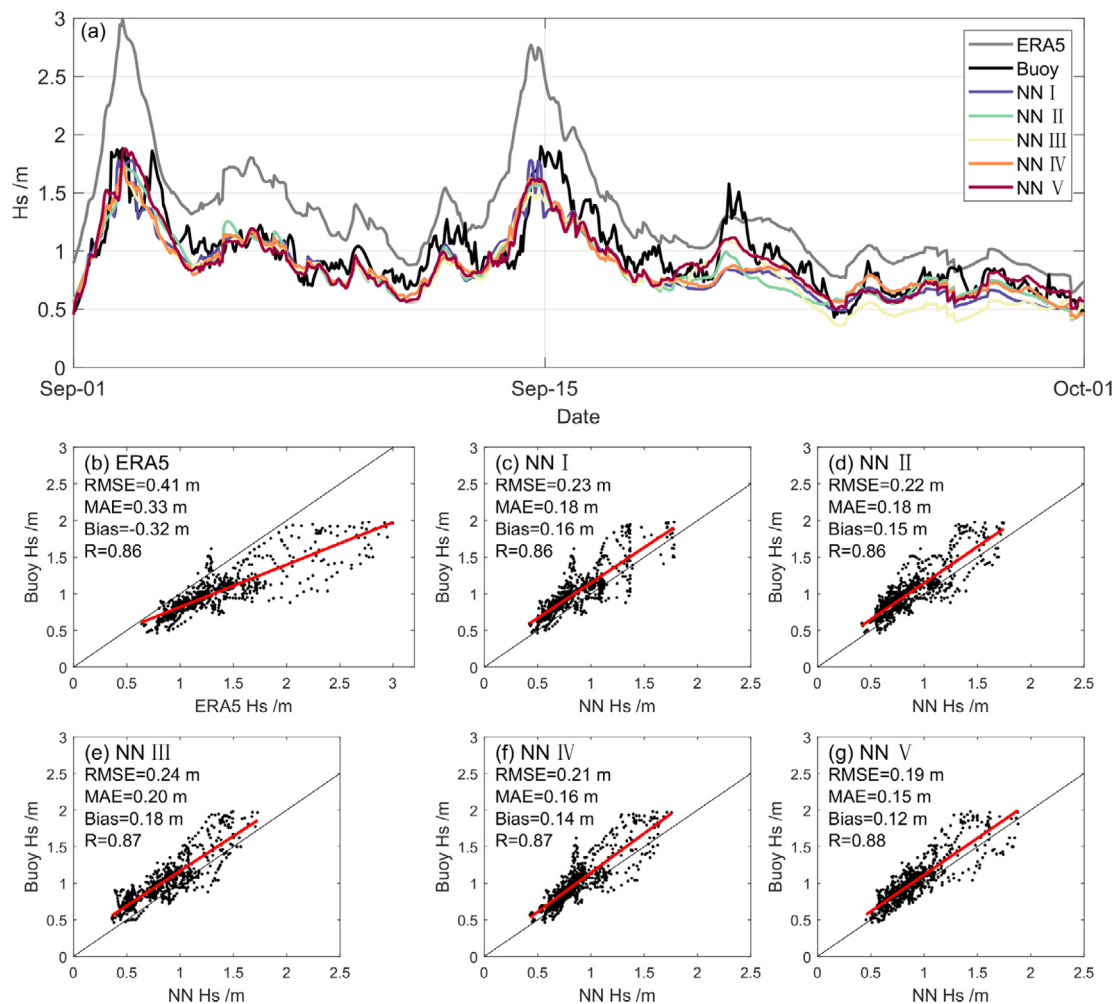
Fig. 5. Comparison of the (a) time series and (b–g) scatter plots of *Hs* between the ANN model results and buoy observations in the verification stage based on Dataset 1 (Table 2).

(Albuquerque et al., 2018; Lu et al., 2019). However, in the ANN models established in this study, additionally considering the wind field, wave direction and other factors did not bring obvious improvement to the calibration effect of *Hs* and *Te* (Figs. 5c–g and 6c–g). This may be because the relationship among variables such as wind field and wave height, direction, and the period has been relatively stable after the modulation of the ERA5 model. Therefore, even if these parameters were supplemented, they did not bring much new information to the ANN models. The current calibration results are close to the best level that can be achieved by using ERA5 data.

Based on the calibration and verification results, models NN H5 and NN T2 are respectively selected to calibrate the ERA5 *Hs* and *Te* data from May to September and the whole month of each year from 1979 to 2020. It is worth mentioning that the ANN-calibrated ERA5 *Hs* from October to April was not adopted in this study. Calibration experiments of the REA5 *Hs* corresponding to these months were also experimentally conducted based on Dataset 2, and all ANN models did not show a distinct calibration effect of the *Hs* (figures omit). Furthermore, the original data were already in good agreement with observations during the periods from November 2018 to April 2019 and from October 2019 to March 2020, representing an RMSE of 0.22 m (Fig. 2e), which is close to that of calibrated *Hs* during the summer monsoon (0.19–0.23 m in Fig. 5). As the wave characteristic here is dominated by the monsoon climate, it can be inferred that the ERA5 *Hs* may also represent a higher accuracy from October to April during

other years. As a result, the original *Hs* from October to April were combined with the calibrated *Hs* from May to September for further wave energy assessment.

3.2. Seasonal and long-term characteristics of the wave energy

The wave energy parameters, including *Pw*, *Cv*, ALF, and RLF, were calculated with calibrated data for the last 40 years. Annually, wave energy is higher and more stable during winter, lower and less stable in summer monsoons, and lowest and least stable in spring (Fig. 7). The variation feature of wave energy is consistent with that of the SCS monsoons (Wyrtki, 1961; Wu and Wang, 2002; Su et al., 2017). The winter monsoon is relatively strong. Accordingly, the *Pw* from October to February is stronger, ALF and RLF are higher, and the stability of wave energy resources is also higher (*Cv* is lower). During these months, the monthly averaged *Pw* is higher than 5 kW m^{-1}, with an ALF higher than 50%. Then, with the weakening of the winter monsoon, the wave energy decreases. In spring, the wave energy resource is poor, and the ALF is low. The annual bottom of *Pw* appears in May. Later, with the outbreak of the summer monsoon, wave energy resources rapidly increased. In general, wave energy potential here is not abundant, especially outside winter, and therefore, a hybrid solution with e.g., offshore wind energy, could be much more feasible.

Clarifying the directional characteristics of wave energy is important to improve the efficiency of WECs (Wang and Lu,
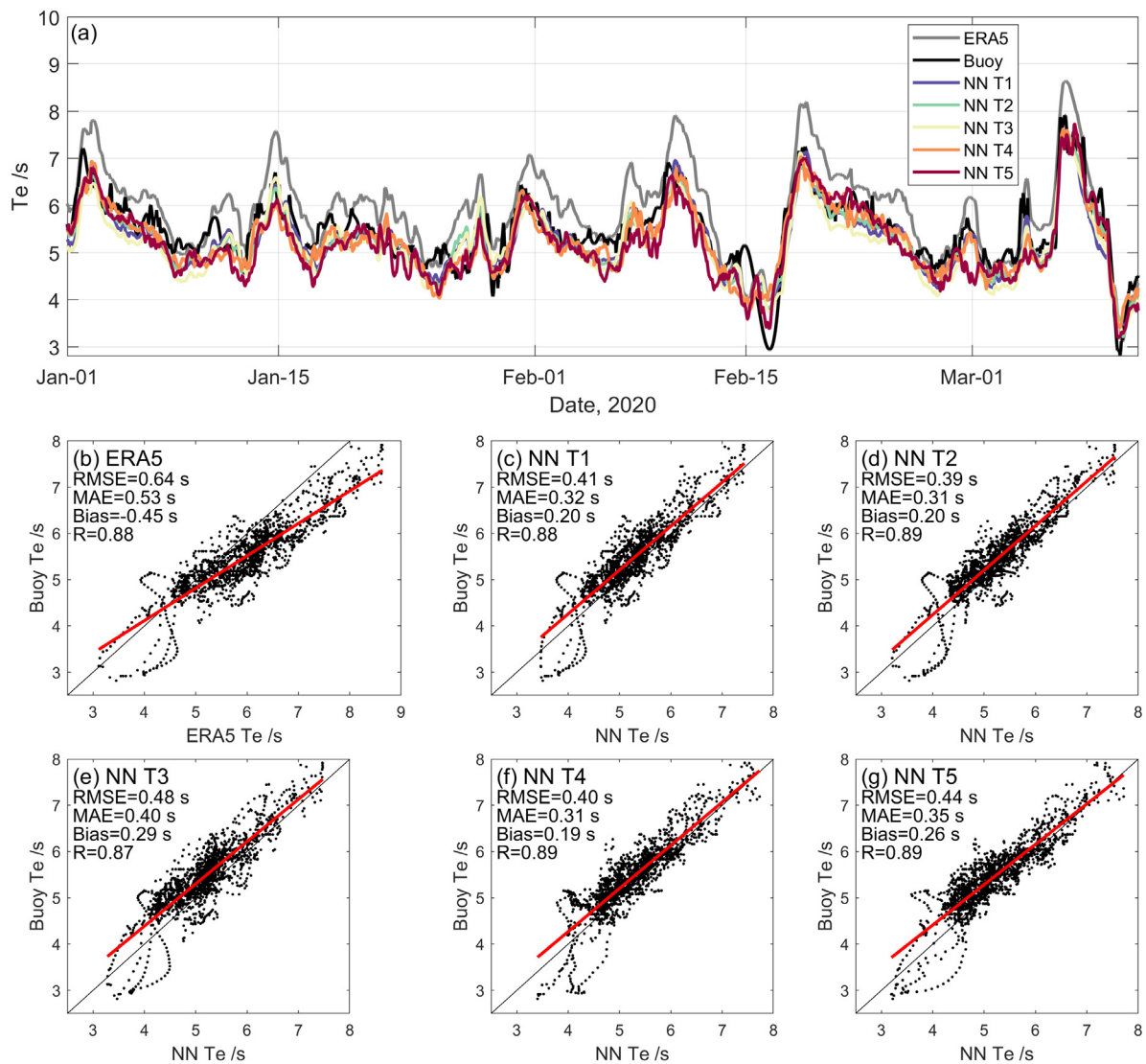
Fig. 6. Similar to Fig. 5 but for *Te* based on Dataset 3.

2009). The percentage of wave occurrence by incoming direction and by wave energy is illustrated by wave roses (Fig. 8). The region experiences a seasonal reversing wave climate. This feature is consistent with the seasonal variation of the SCS monsoons, where the wind directions reverse seasonally (Wyrtki, 1961; Wu and Wang, 2002). The wave energy is concentrated during summer and winter, with the energy coming from the N-E quadrant and the S-W quadrant, respectively. Annually, the most occurring wave energy mainly comes from NNE and WSW, which both account for more than 20% of the total energy. The wave energy of more than 20 kW m^{-1} mostly comes from the NNE and N directions, which occurs in autumn and winter. In summer, most wave energy has a higher occurrence from WSW, accounting for more than 60% of the total. In autumn, as the summer monsoon decays and the winter monsoon rises, wave energy propagations from NNE and WSW coexist. Such seasonal variations should be fully considered in the design and deployment of WECs in the SSCS.

The combined scatter and energy diagrams of *Hs* and *Te* based on the monthly average data from 1979 to 2019 (Fig. 9) provide comprehensive information on the occurrence frequency of wave energy resources. The annual mean diagram shows that the bins from 0.5–3 m in *Hs* and 4–8 s in *Te* provide outstanding contributions (~70%) to the total energy. The wave energy in summer and

winter, compared with those in spring and autumn, tends to be distributed in sea states with higher *Hs* and *Te*. The *Pw* bins exceeding 10 kW m^{-1} are more widely distributed in winter than in other seasons, suggesting stronger wave energy during that time. According to Stopa et al. (2013), wave power with a minimum of 5 kW m^{-1} combined with a median value of 12 kW m^{-1} is highly desired for WEC devices. The *Hs-Te* bins with outstanding contributions to the total energy in Fig. 9e are basically above the isoline of 5 kW m^{-1}. However, they are seldom exceeding 12 kW m^{-1}, and far less than those in the Irish seas, Atlantic, Scotland where the energy fluxes can be high as an order of 30–50 kW m^{-1} (Reeve et al., 2011; Young et al., 2011). The results suggest a possible shortage for wave energy farming via WECs, and a hybrid solution with offshore wind energy, current energy, and solar energy (Li et al., 2022a; Pérez-Collazo et al., 2015; Widén et al., 2015) would be more suitable for the area.

It is noteworthy that the diagrams also indicate that the largest contribution of wave energy does not correspond to the bins with the largest occurrence; likewise, the bins with the largest occurrence do not necessarily provide the largest contribution. For example, the highest annual energy percentage occurs when *Hs* and *Te* lie in the interval of 2.0–2.5 (m) and 6–7 (s), accounting for 13.0% of the total energy, while the occurrence number in the
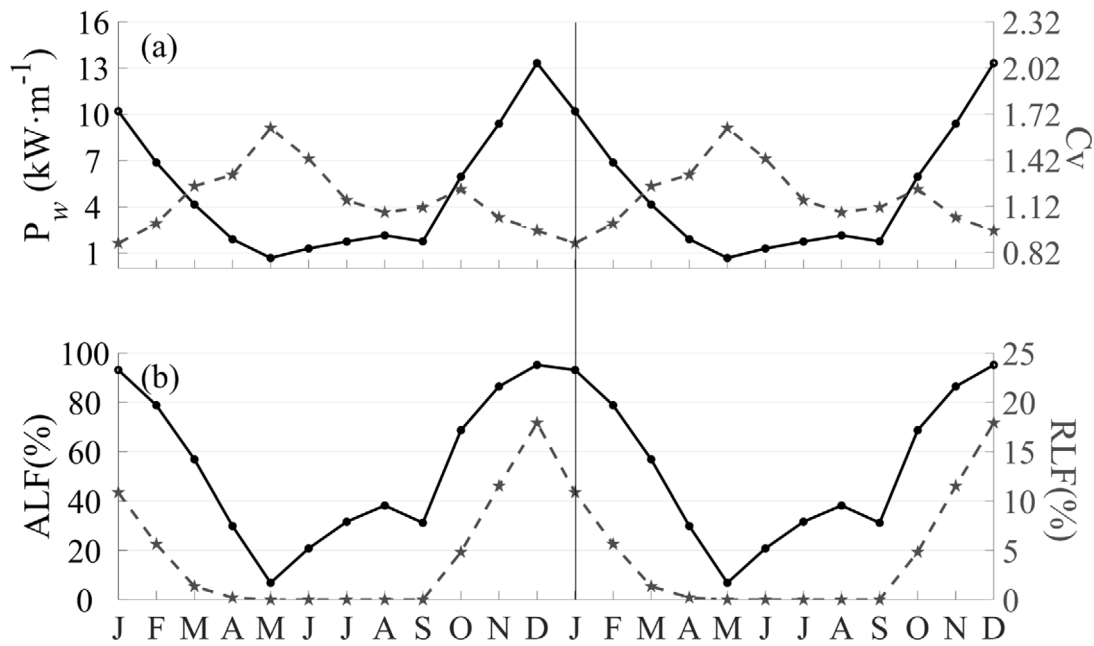
Fig. 7. Multiyear (1979–2019) monthly averages of wave energy density (P_w, black solid line in a), coefficient of variation (Cv, gray dotted line in a), wave energy available level frequency (ALF, black solid line in b), and rich level frequency (RLF, gray dotted line in b).
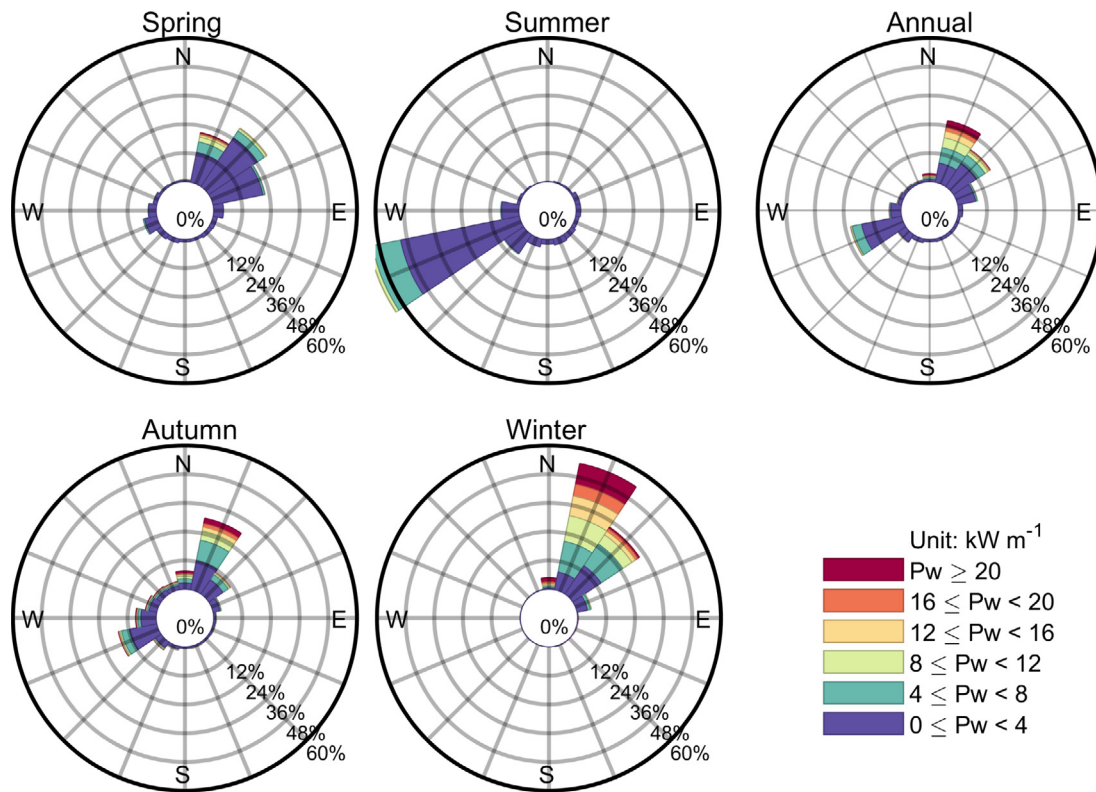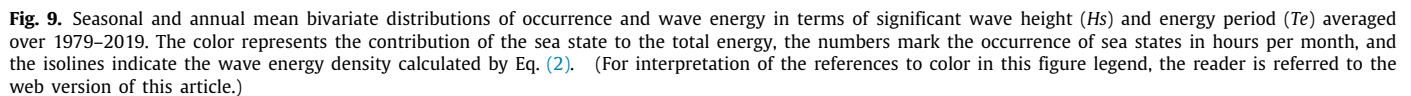

Fig. 8. Seasonal and annual wave energy roses averaged over 1979–2019.

interval is 28 h per month, which is not the most frequent among all intervals (Fig. 9e). This characteristic can provide an important reference for the design of a WEC to meet the needs of energy acquisition.

The long-term variation analysis shows a continuous growth trend of the wave energy resources in the SSCS in the last 40 years (Fig. 10). The annual averaged ALF is continuous at no less than 40%, and Cv has little long-term trend with high interannual fluctuations between 1.2 and 2.2. The Pw, ALF, and RLF show significant increasing trends of 0.027 kW m^{-1}, 0.12%, and 0.05% per year, with P values equal to 0.003, 0.032, and 0.027, respectively. The results of Zheng (2021) integrated several sets of reanalysis data showed that the growth trend of wave energy in the SSCS is about 0.02–0.04 kW m^{-1} per year, which is consistent with the trend proposed in this paper. It should also be pointed out that the trend of wave energy resources in the SSCS is not high

Fig. 9. Seasonal and annual mean bivariate distributions of occurrence and wave energy in terms of significant wave height (*Hs*) and energy period (*Te*) averaged over 1979–2019. The color represents the contribution of the sea state to the total energy, the numbers mark the occurrence of sea states in hours per month, and the isolines indicate the wave energy density calculated by Eq. (2). (For interpretation of the references to color in this figure legend, the reader is referred to the web version of this article.)

compared with the Indian Ocean and the Western Pacific, whose annual increasing rate of wave energy is as high as 0.06–0.12 kW m^{-1} per year and 0.15 kW m^{-1} per year (Zheng, 2021).

Such a growing trend can be related to global climate change. In recent years, probably as a consequence of oceanic warming, global wave height in extreme conditions (90th percentiles) has been increasing (Young and Ribal, 2019), the average wind speed and wave energy resources in global oceans have shown obvious increasing trends (Thomas et al., 2008; Young et al., 2011; Zheng and Li, 2015; Zheng, 2021). Further analysis in the wind field variations indicates that the rising trend of wave energy in the SSCS is related to the enhancement of waves generated and propagated from the northeast region of the SCS near the Luzon Strait (Fig. 11). It can be seen from the figure that the wind speed in the SSCS near the study site has not changed significantly in the last 40 years. In contrast, the wind speed in

the northeastern SCS near the Luzon Strait shows a significant upward trend during these years. Previous studies have shown that the most obvious rising trend of wave energy in the SCS lies in the northeast region, and the growth trend extends from northeast to southwest (Zheng and Li, 2015). In the SSCS, the swell propagating from northeast to southwest dominates the wave composition (Su et al., 2017). Therefore, the growth trend of waves in the northeast can gradually spread to the SSCS in the form of swell propagation.

In comparison, in some relatively closed regions such as the Persian Gulf and Mediterranean sea, the changing trend of wave energy resources is relatively insensitive to the local wind speed, probably due to the limitation of the wind zone distance (Emmanouil et al., 2016). Moreover, a decadal change of wind direction to the land frontier can obstruct the development of waves and thus lead to a long-term decrease in wave energy (Kamranzad
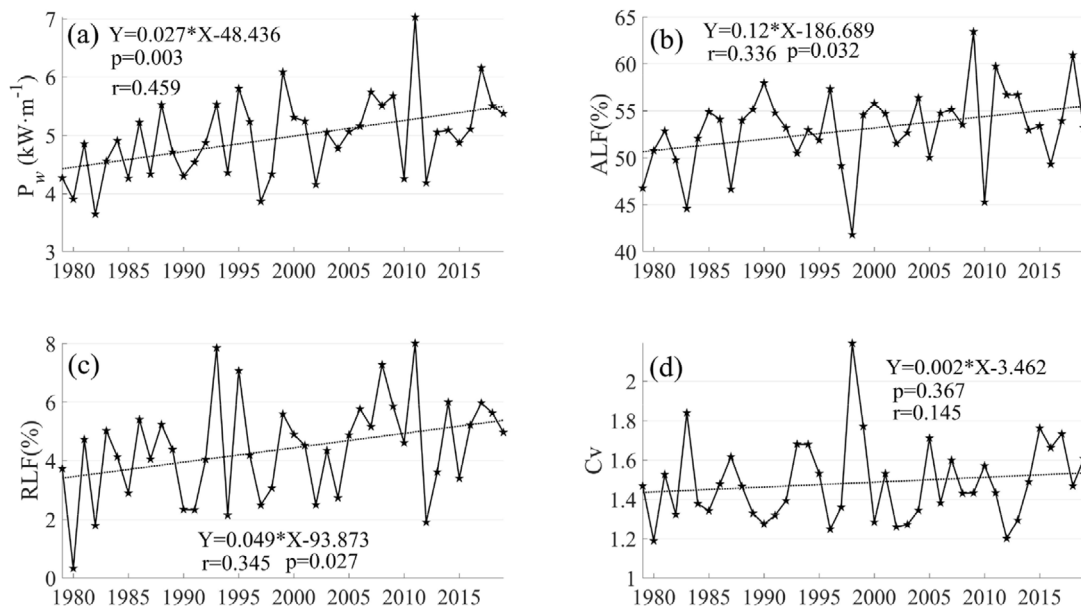
Fig. 10. Long-term (1979–2019) trends in annual average (a) wave energy density (P_w), (b) available level frequencies (ALF), (c) rich level frequencies (RLF), and (d) coefficient of variation (Cv).
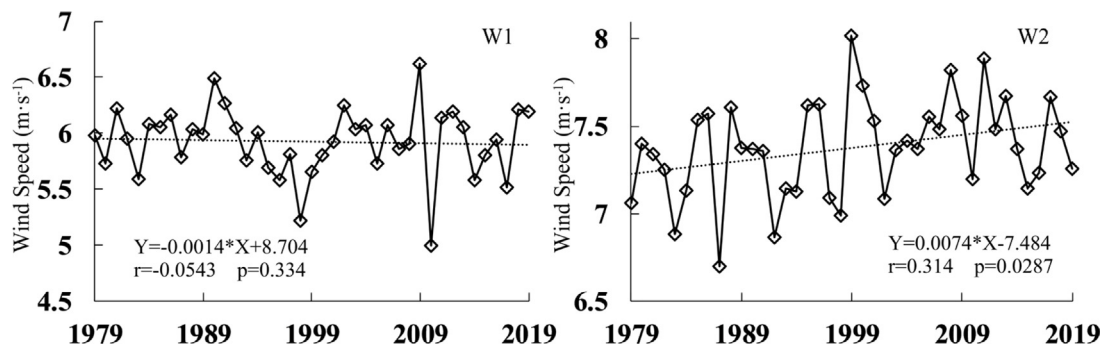
Fig. 11. Long-term (1979–2019) trends of annual average wind speed in (left panel) the southern and (left panel) the northeastern South China Sea. The calculation regions correspond to the red boxes (W1 and W2) in Fig. 1.

et al., 2013). By contraries, the SCS has a wide enough sea area to spread the wave energy growing in the northeast to the SSCS.

### 3.3. Significance of data calibration for the wave energy assessment

To analyze the possible errors caused by the use of uncalibrated data to assess wave energy, the seasonal and long-term variations in wave energy calculated in the above section are reanalyzed by using the original ERA5 data that are not calibrated by any models. The results show that there are significant differences between the assessment results of the calibrated data and the original data (Fig. 12). For example, the Pw, ALF, and RLF calculated by uncalibrated data are higher than those calculated by calibrated data (Fig. 12a and b). Taking the results of summer as an example, the Pw and ALF are overestimated by using uncalibrated data with 1.8 kW m^{-1} and 9.7%, respectively, compared with the results of calibrated data. For the long-term variations, although calculation using the uncalibrated data would not misjudge the significant increasing trend of wave energy resources, it will overestimate the magnitude of the trend (Fig. 12c). According to the results of the calibrated data, the ALF increases by 0.12% per year. If the data were not calibrated, the rate became 0.18% per year, which was overestimated by 50%. These results indicate that if the wave energy was assessed based on uncalibrated data, the

results could become too optimistic, which may lead to a waste of investment in energy development.

Moreover, the bivariate distributions of occurrence and wave energy in terms of Hs and Te may be misunderstood by the uncalibrated data (Fig. 13). The analysis shows that the main energy is generally concentrated in waves of 0.5–3 m height, regardless of whether the data are calibrated or not. However, based on the uncalibrated data, the wave energy with a relatively short period (3–6 s) would be underestimated, while the wave energy with a relatively long period (6–11 s) would be overemphasized. If inaccurate parameter information is used in the design of WECs, it may lead to devices being unable to achieve their optimal capacity. Therefore, whether the data are calibrated will affect the judgment of the wave energy level and the reasonable design of the WEC.

3.4. Implications for wave energy assessment in other multi-island regions

There are many islands and reefs in the SCS (Fig. 1). The installation of WECs is often close to islands so that the costs will not be too high and can be profitable for communities. Numerical models can provide long-term series of wave parameter information, so they are widely used in wave energy assessments (Zheng et al., 2012, 2013; Ali et al., 2015; Wan et al., 2018; Wang
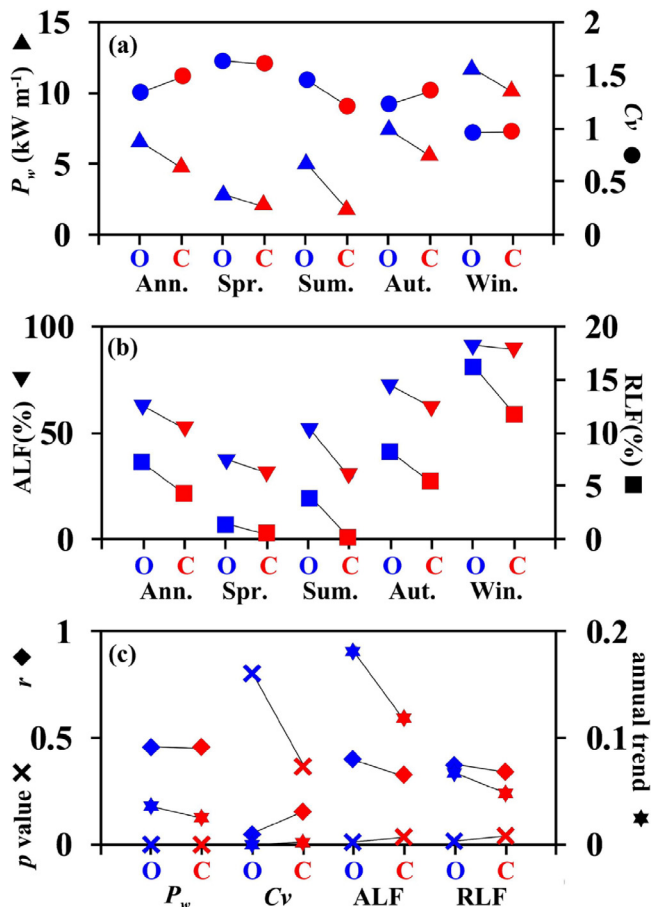
Fig. 12. Comparison of wave energy parameters calculated by original ERA5 data (plots in blue) and by date calibrated by buoy observations using neural network models (plots in red). (a) is the annual and seasonal mean of wave energy density (P_w) and coefficient of variation (Cv), (b) is the annual and seasonal mean of available level frequencies (ALF) and rich level frequencies (RLF), and (c) is the annual trend of P_w, ALF, RLF and Cv, and their correlation coefficients (r) and p values with year. (For interpretation of the references to color in this figure legend, the reader is referred to the web version of this article.)

et al., 2018; Lin et al., 2019; Sun et al., 2020). However, in multi-island regions, the reliability of model data may need to be fully validated.

Our results mainly indicate that it is necessary to calibrate the model data when evaluating wave energy in multi-island regions. There was a significant difference between the ERA5 model data and field observations at our study site (Fig. 2). The main reason for the difference may be that the model does not have enough spatial resolution to characterize the topography of islands and reefs. By comparing the models of Wang et al. (2018) and Sun et al. (2020), it can be found that the island's resistance to waves is relatively obvious in the higher-resolution model. If the reef terrains cannot be distinguished, the wave propagation distance in the model will be longer than the actual distance, so the component of the swell will be larger, which increases the model values of Te (Fig. 2). In addition, the waves in the SCS are affected by the monsoons, with waves from the NE dominating during the winter monsoon and those from the SW dominating during the summer monsoon (Wyrtki, 1961; Wu and Wang, 2002; Su et al., 2017). As the site is relatively close to a reef in the south and relatively open in the north (Fig. 1), the waves are more susceptible to shallowing and diffraction during the summer monsoon, resulting in a decrease in Hs (Fig. 2). With the improvement of numerical simulation technology and

the increase in computing resources, the spatial resolution of the numerical model is increasing. However, although the 5–7 km resolution model can simulate relatively large reefs in the Xisha Islands and Zhongsha Islands (Sun et al., 2020), the spatial scale of dotted reefs in the Nansha region is mostly less than 1 km (Jiang et al., 2018). These reefs are still difficult to identify effectively in most numerical models.

Our results verify the effectiveness of the ANN method to calibrate model data and then evaluate wave energy in multi-island regions (Figs. 4–10). Previous studies have shown that the ANN model is effective for wave model calibration and wave energy assessments (Reikard et al., 2011; Hadadpour et al., 2014; Sánchez et al., 2018; Avila et al., 2020; Li et al., 2020). However, because it is difficult to obtain long-series wave observations for remote island regions, the existing studies combining models and in situ data are mostly performed in nearshore regions. Although only one site is deployed in this study, the typical example can be extended to other multi-island regions. For other sites, the azimuth and distance of surrounding reefs may affect the variations in model bias. For example, the area south of our site is relatively close to reefs (Fig. 1), which results in a larger model bias during the summer monsoon when waves propagate from the SW (Fig. 2). Moreover, our site is located in the center of a multi-island region where swells from all directions can be largely blocked (Fig. 1). Thus, the wave period from the models would be larger than the true value, which may affect the accuracy of the wave energy calculation. Although most studies focus on Hs, the calibration of Te is particularly important in this study (Fig. 13). Therefore, it is necessary to establish an appropriate ANN model according to the actual situation for a certain site.

4. Conclusion

In this study, the wave energy resources of a typical site in a multi-island region in the southern South China Sea (SSCS) were systematically analyzed by integrating model-based ERA5 data from 1979–2020 and field observation data for a year and a half. Combined with the observation data of a buoy deployed in the SSCS, artificial neural network (ANN) models were established to calibrate ERA5 reanalysis data over nearly 40 years. The verification results showed that the calibrated significant wave height and mean wave period are in good agreement with the observation data.

The seasonality and long-term trend of wave energy resources are systematically analyzed based on the data. Analysis results indicate that due to the influence of monsoons, the wave energy resources in the SSCS show significant seasonal variations. Wave energy is higher and more stable in winter (with an average energy density higher than 5 kW m^{-1} and an available level frequency higher than 50% from October to February), lower and less stable in the summer monsoon, and lowest and least stable in spring. In general, wave energy potential here is not abundant, and a hybrid solution with offshore wind energy, current energy, and solar energy would be more suitable for the area.

There are obvious variations in the characteristics of wave height, wave period, and wave direction for the energy resources in different seasons. On the long-term scale, the intensity, availability, and stability of wave energy resources have shown an upward trend in the last 40 years. Particularly, wave power density in the SSCS shows significant increasing trends of 0.027 kW m^{-1} per year. The rising trend is consistent with the enhancement of wind speed near the Luzon Strait, suggesting the growth trend of waves in the northeast region of the SCS can gradually spread to the SSCS in the form of swell propagation.

The presented example can provide a reference for the evaluation of wave energy in other multi-island regions. By comparing
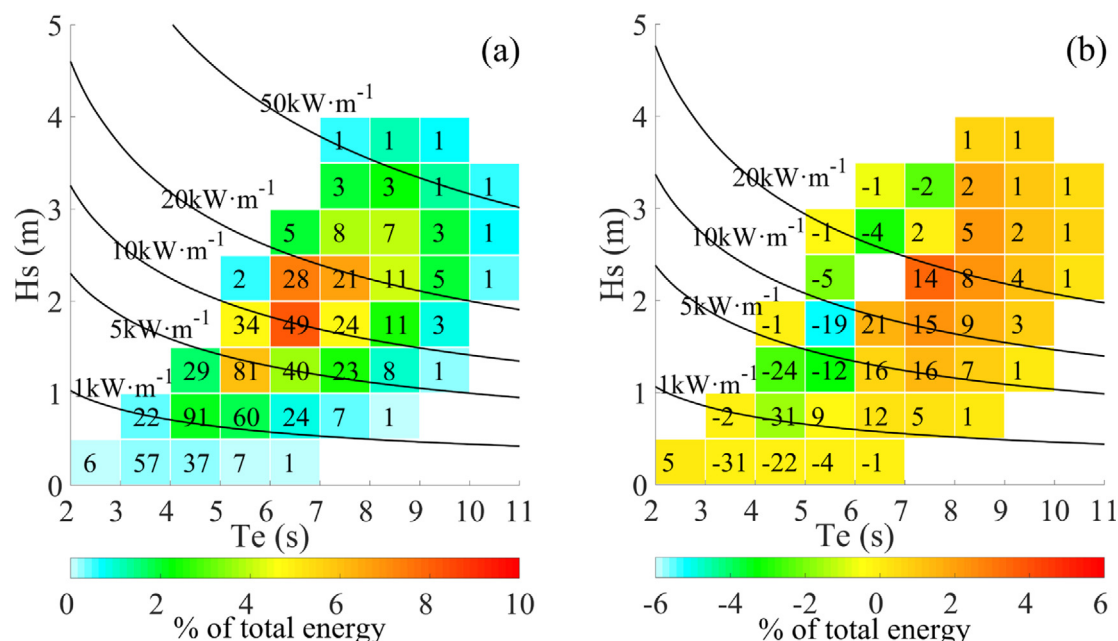
Fig. 13. (a) Same as Fig. 9e but calculated based on original reanalysis data; (b) the difference between Fig. 12a minus Fig. 9e.

the results of wave energy assessments with calibrated or uncalibrated data, it is found that if the data are not calibrated, the wave energy level may be overestimated, and the magnitude of its long-term trend may be misjudged, thus misleading the design of power generation equipment. Therefore, when planning and utilizing wave energy resources, it is necessary to fully consider the reliability of the data and correct the data effectively by certain methods. Artificial intelligence technology is expected to provide a fast and convenient tool for the correction of such data.

CRediT authorship contribution statement

Bo Li: Formal analysis, Methodology, Validation, Writing – original draft. **Wuyang Chen:** Data curation, Visualization. **Junmin Li:** Conceptualization, Resources, Supervision, Writing – review & editing. **Junliang Liu:** Investigation. **Ping Shi:** Funding acquisition. **Huanlin Xing:** Investigation.

Declaration of competing interest

The authors declare that they have no known competing financial interests or personal relationships that could have appeared to influence the work reported in this paper.

Acknowledgments

References

Albuquerque, J., Antolínez, J.A.A., Rueda, A., Méndez, F.J., Coco, G., 2018. Directional correction of modeled sea and swell wave heights using satellite altimeter data. Ocean Model. 131, 103–114. http://dx.doi.org/10.1016/j.ocemod.2018.09.001.

Ali, M., Fredolin, T., Liew, J., 2015. Wave energy potential assessment in the central and southern regions of the South China Sea. Renew. Energy 80, 454–470. http://dx.doi.org/10.1016/j.renene.2015.02.005.

Andréfouët, S., Ardhuin, F., Queffeulou, P., Gendre, R.L., 2012. Island shadow effects and the wave climate of the Western Tuamotu Archipelago (French Polynesia) inferred from altimetry and numerical model data. Mar. Pollut. Bull. 65, 415–424. http://dx.doi.org/10.1016/j.marpolbul.2012.05.042.

Avila, D., Marichal, G.N., Padrón, I., Quiza, R., Hernández, N., 2020. Forecasting of wave energy in Canary Islands based on artificial intelligence. Appl. Ocean Res. 101, 102189. http://dx.doi.org/10.1016/j.apor.2020.102189.

Beale, M., Hagan, M.T., Demuth, H.B., 2010. Neural Network Toolbox 7 - User's Guide. MathWorks, Natick, Mass, p. 951.

Bedard, R., Wave Energy Forecasting Accuracy As a Function of Forecast Time Horizon: A Case Study of the NOAA Wavewatch III TM Wind/Wave Forecast Model Wave Parameter Results Compared to Measurements at NOAA NDBC Data Buoy (46027) which is in 48m depth water near the Oregon-California Border (a depth typical of Oregon and Northern California Wave Power Plant Locations). EPRI-WP-013, Paolo, Alto, CA.

Bento, P.M.R., Pombo, J.A.N., Mendes, R.P.G., Calado, M.R.A., Mariano, S.J.P.S., 2021. Ocean wave energy forecasting using optimised deep learning neural networks. Ocean Eng. 219, 108372. http://dx.doi.org/10.1016/j.oceaneng.2020.108372.

Bromirski, P.D., Cayan, D.R., Helly, J., Wittmann, P., 2013. Wave power variability and trends across the North Pacific. J. Geophys. Res. Oceans 118, 6329–6348. http://dx.doi.org/10.1002/2013JC009189.

Chen, X., Wang, K., Zhang, Z., Zeng, Y., Zhang, Y., O'Driscoll, K., 2017. An assessment of wind and wave climate as potential sources of renewable energy in the nearshore Shenzhen coastal zone of the South China Sea. Energy 134, 789–801. http://dx.doi.org/10.1016/j.energy.2017.06.043.

Cornett, A.M., 2008. A global wave energy resource assessment. In: Proceedings of 18th International Conference on Offshore and Polar Engineering. The International Society of Offshore and Polar Engineers, BC, Canada, Vancouver.

Deo, M.C., Naidu, C.S., 1998. Real time forecasting using neural networks. Ocean Eng. 26, 191–203. http://dx.doi.org/10.1016/S0029-8018(97)10025-7.

ECMWF, 2021. IFS documentation CY47r3 - Part VII: ECMWF wave model. https://www.ecmwf.int/node/20201.

Emmanouil, G., Galanis, G., Kalogeri, C., Zodiatis, G., Kallos, G., 2016. 10-Year high resolution study of wind, sea waves and wave energy assessment in the Greek offshore areas. Renew. Energy 90, 399–419. http://dx.doi.org/10.1016/j.renene.2016.01.031.

Fett, R.W., Kevin, M.R., 1976. Island barrier effect on sea state as revealed by a numerical wave model and DMSP satellite data. J. Phys. Oceanogr. 6, 324–334. http://dx.doi.org/10.1175/1520-0485(1976)0062.0.CO;2.

Guenaydin, K., 2008. The estimation of monthly mean significant wave heights by using artificial neural network and regression methods. Ocean Eng. 35, 1406–1415. http://dx.doi.org/10.1016/j.oceaneng.2008.07.008.

Gunn, K., Stockwilliams, C., 2012. Quantifying the global wave power resource. Renew. Energy 44, 296–304. http://dx.doi.org/10.1016/j.renene.2012.01.101.

Hadadpour, S., Etemad-Shahidi, A., Kamranzad, B., 2014. Wave energy forecasting using artificial neural networks in the Caspian Sea. Proc. ICE: Marit. Eng. 167, 42–52. http://dx.doi.org/10.1680/maen.13.00004.

Hersbach, H., Bell, B., Berrisford, P., Biavati, G., Horányi, A., Muñoz Sabater, J., Nicolas, J., Peubey, C., Radu, R., Rozum, I., Schepers, D., Simmons, A., Soci, C., Dee, D., Thépaut, J.-N., 2018. ERA5 hourly data on single levels from 1979 to present. In: Copernicus Climate Change Service (C3S) Climate Data Store (CDS). http://dx.doi.org/10.24381/cds.adbb2d47, (Accessed on < 31-December-2021 >).

Iglesias, G., López, M., Carballo, R., Castro, A., Fraguela, J.A., Frigaard, P., 2009. Wave energy potential in Galicia (NW Spain). Renew. Energy 34, 2323–2333. http://dx.doi.org/10.1016/j.renene.2009.03.030.

Jiang, H., Su, F., Zhou, C., Yang, X., Wang, Q., Cheng, F., 2018. The geographical characteristics of Nansha Islands in the South China Sea. J. Geogr. Sci. 28, 957–972. http://dx.doi.org/10.1007/s11442-018-1515-8.

Kamranzad, B., Etemad-shahidi, A., Chegini, V., 2013. Assessment of wave energy variation in the Persian Gulf. Ocean Eng. 70, 72–80. http://dx.doi.org/10.1016/j.oceaneng.2013.05.027.

Ponce de León, S., Soares, C.G., 2005. On the sheltering effect of islands in ocean wave models. J. Geophys. Res. Oceans 110, C09020. http://dx.doi.org/10.1029/2004jc002682.

Li, B., Chen, W., Li, J., Liu, J., Shi, P., 2022a. Integrated monitoring and assessments of marine energy for a small uninhabited island. Energy Rep. 8, 63–72. http://dx.doi.org/10.1016/j.egyr.2022.01.114.

Li, B., Li, J., Li, Y., Zhang, Z., Shi, P., Liu, J., Chen, W., 2020. Application of artificial neural network to numerical wave simulation in the coastal region of island. J. Xiamen Univ. Nat. Sci. 59, 420–427. http://dx.doi.org/10.6043/j.issn.0438-0479.201908035, (in Chinese).

Li, B., Li, J., Liu, J., Tang, S., Chen, W., Shi, P., Liu, Y., 2022b. Calibration experiments of CFOSAT wavelength in the Southern South China Sea by artificial neural networks. Remote Sens. 14 (3), 773. http://dx.doi.org/10.3390/rs14030773.

Lin, Y., Dong, S., Wang, Z., Guedes Soares, C., 2019. Wave energy assessment in the China adjacent seas on the basis of a 20-year SWAN simulation with unstructured grids. Renew. Energy 136, 275–295. http://dx.doi.org/10.1016/j.renene.2019.01.011.

Londhe, S.N., Shah, S., Dixit, P.R., Nair, T.M.B., Sirisha, P., Jain, R., 2016. A coupled numerical and artificial neural network model for improving location specific wave forecast. Appl. Ocean Res. 59, 483–491. http://dx.doi.org/10.1016/j.apor.2016.07.004.

Lu, W., Su, H., Yang, X., Yan, X.H., 2019. Subsurface temperature estimation from remote sensing data using a clustering-neural network method. Remote Sens. Environ. 422, 213–222. http://dx.doi.org/10.1016/j.rse.2019.04.009.

Macisaac, C., Naeth, S., 2014. TRIAXYS Next wave II directional wave sensor. The evolution of wave measurements. In: Oceans. MTS.

Mao, K., Chen, X., Wang, L., 2014. Research progress of spectral wave mode of archipelago or reef ocean region. Acta Oceanol. Sin. 36, 161–169. http://dx.doi.org/10.3969/j.issn.0253-4193.2014.05.018, (in Chinese).

Pérez-Collazo, C., Greaves, D., Iglesias, G., 2015. A review of combined wave and offshore wind energy. Renew. Sustain. Energy Rev. 42, 141–153. http://dx.doi.org/10.1016/j.rser.2014.09.032.

Reeve, D.E., Chen, Y., Pan, S., Magar, V., Simmonds, D.J., Zacharioudaki, A., 2011. An investigation of the impacts of climate change on wave energy generation: The Wave Hub, Cornwall, UK. Renew. Energy 36, 2404–2413. http://dx.doi.org/10.1016/j.renene.2011.02.020.

Reikard, G., Pinson, P., Bidlot, J.R., 2011. Forecasting ocean wave energy: The ECMWF wave model and time series methods. Ocean Eng. 38, 1089–1099. http://dx.doi.org/10.1016/j.oceaneng.2011.04.009.

Sánchez, A., Rodrigues, D.A., Fontes, R.M., Martins, M.F., Kalid, R.D.A., Torres, E.A., 2018. Wave resource characterization through in-situ measurement followed by artificial neural networks' modeling. Renew. Energy 115, 1055–1066. http://dx.doi.org/10.1016/j.renene.2017.09.032.

Stopa, J.E., Filipot, J.F., Li, N., Cheung, K.F., Chen, Y.L., Vega, L., 2013. Wave energy resources along the Hawaiian Island chain. Renew. Energy 55, 305–321. http://dx.doi.org/10.1016/j.renene.2012.12.030.

Su, H., Wei, C., Jiang, S., Li, P., Zhai, F., 2017. Revisiting the seasonal wave height variability in the South China Sea with merged satellite altimetry observations. Acta Oceanol. Sin. 36, 38–50. http://dx.doi.org/10.1007/s13131-017-1073-4.

Sun, Z., Zhang, H., Liu, X., Ding, J., Cai, Z., 2021. Wave energy assessment of the Xisha Group Islands zone for the period 2010–2019. Energy 220, 119721. http://dx.doi.org/10.1016/j.energy.2020.119721.

Sun, Z., Zhang, H., Xu, D., Liu, X., Ding, J., 2020. Assessment of wave power in the South China Sea based on 26-year high-resolution hindcast data. Energy 197, 117218. http://dx.doi.org/10.1016/j.energy.2020.117218.

Taylor, K.E., 2001. Summarizing multiple aspects of model performance in a single diagram. J. Geophys. Res. Atmos. 106, 7183–7192. http://dx.doi.org/10.1029/2000JD900719.

Thomas, B.R., Kent, E.C., Swail, V.R., Berry, D.I., 2008. Trends in ship wind speeds adjusted for observation method and height. Int. J. Climatol. 28, 747–763. http://dx.doi.org/10.1002/joc.1570.

Thrasher, B., Maurer, E., McKellar, C., Duffy, P., 2012. Technical Note: Bias correcting climate model simulated daily temperature extremes with quantile mapping. Hydrol. Earth Syst. Sci. 16, 3309–3314. http://dx.doi.org/10.5194/hessd-9-5515-2012.

Tolman, H., 2003. Treatment of unresolved islands and ice in wind wave models. Ocean Model. 5, 219–231. http://dx.doi.org/10.1016/S1463-5003(02)00040-9.

Wan, Y., Fan, C., Dai, Y., Li, L., Sun, W., Zhou, P., Qu, X., 2018. Assessment of the joint development potential of wave and wind energy in the South China Sea. Energies 11, 1–26. http://dx.doi.org/10.3390/en11020398.

Wan, Y., Zhang, J., Meng, J.M., Wang, J., 2015. Exploitable wave energy assessment based on ERA-interim reanalysis data — A case study in the East China Sea and the South China Sea. Acta Oceanol. Sin. 34, 143–155. http://dx.doi.org/10.1007/s13131-015-0641-8.

Wang, Z., Duan, C., Dong, S., 2018. Long-term wind and wave energy resource assessment in the South China sea based on 30-year hindcast data. Ocean Eng. 163, 58–75. http://dx.doi.org/10.1016/j.oceaneng.2018.05.070.

Wang, C.K., Lu, W., 2009. Analysis Methods and Reserves Evaluation of Ocean Energy Resources. Ocean Press, Beijing, China, pp. 104–129.

Widén, J., Carpman, N., Castellucci, V., Lingfors, D., Olauson, J., Remouit, F., Bergkvist, M., Grabbe, M., Waters, R., 2015. Variability assessment and forecasting of renewables: A review for solar, wind, wave and tidal resources. Renew. Sustain. Energy Rev. 44, 356–375. http://dx.doi.org/10.1016/j.rser.2014.12.019.

Wood, A.W., Maurer, E.P., Kumar, A., Lettenmaier, D.P., 2002. Long-range experimental hydrologic forecasting for the eastern United States. J. Geophys. Res. Atmos. 107 (4429), http://dx.doi.org/10.1029/2001JD000659.

Wu, S., Liu, C., Chen, X., 2015. Offshore wave energy resource assessment in the East China Sea. Renew. Energy 76, 628–636. http://dx.doi.org/10.1016/j.renene.2014.11.054.

Wu, B., Wang, J., 2002. Possible impacts of winter arctic oscillation on Siberian high, the East Asian winter monsoon and sea–ice extent. Adv. Atmos. Sci. 19, 297–320. http://dx.doi.org/10.1007/s00376-002-0024-x.

Wyrtki, K., 1961. Physical Oceanography of the Southeast Asian Waters: Scientific Results of Marine Investigations of the South China Sea and the Gulf of Thailand, Vol. 2. NAGA Rep. Scripps Inst. Oceanogr., La Jolla, Calif, p. 195.

Young, I.R., Ribal, A., 2019. Multiplatform evaluation of global trends in wind speed and wave height. Science 364, 548–552. http://dx.doi.org/10.1126/science.aav9527.

Young, I.R., Zieger, S., Babanin, A.V., 2011. Global trends in wind speed and wave height. Science 332, 451–455. http://dx.doi.org/10.1126/science.1197219.

Zheng, C.-w., 2021. Global oceanic wave energy resource dataset—with the Maritime Silk Road as a case study. Renew. Energy 169, 843–854. http://dx.doi.org/10.1016/j.renene.2021.01.058.

Zheng, C.W., Li, C.Y., 2015. Variation of the wave energy and significant wave height in the China Sea and adjacent waters. Renew. Sustain. Energy Rev. 43, 381–387. http://dx.doi.org/10.1016/j.rser.2014.11.001.

Zheng, C.W., Pan, J., Li, J.X., 2013. Assessing the China Sea wind energy and wave energy resources from 1988 to 2009. Ocean Eng. 65, 39–48. http://dx.doi.org/10.1016/j.oceaneng.2013.03.006.

Zheng, C.W., Zhuang, H., Li, X., Li, X.Q., 2012. Wind energy and wave energy resources assessment in the east china sea and south china sea. Sci. China Technol. Sci. 55, 163–173. http://dx.doi.org/10.1007/s11431-011-4646-z.